

Article

Defect Prevention in Selective Laser Melting Components: Compositional and Process Effects

Hossein Eskandari Sabzi and Pedro E. J. Rivera-Díaz-del-Castillo *

Department of Engineering, Lancaster University, Gillow Ave, Bailrigg, Lancaster LA1 4YW, UK;
h.eskandarisabzi@lancaster.ac.uk

* Correspondence: p.rivera1@lancaster.ac.uk

Received: 14 October 2019; Accepted: 13 November 2019; Published: 18 November 2019



Abstract: A model to predict the conditions for printability is presented. The model focuses on crack prevention, as well as on avoiding the formation of defects such as keyholes, balls and lack of fusion. Crack prevention is ensured by controlling the solidification temperature range and path, as well as via quantifying its ability to resist thermal stresses upon solidification. Defect formation prevention is ensured by controlling the melt pool geometry and by taking into consideration the melting properties. The model's core relies on thermodynamics and physical analysis to ensure optimal printability, and in turn offers key information for alloy design and selective laser melting process control. The model is shown to describe accurately defect formation of 316L austenitic stainless steels reported in the literature.

Keywords: additive manufacturing; solidification cracking; porosity; austenitic stainless steel

1. Introduction

In additive manufacturing (AM), printability defines the ability of a feedstock to be successfully deposited on a substrate as a bulk material, avoiding significant defects, whilst achieving desired mechanical properties [1]. Printability can be compared to the concept of weldability, which shows the possibility and easiness of two alloys to be welded. However, unlike welding technology, there is not a comprehensive methodology to define the printability of a material under different metallurgical and process conditions.

Powder bed fusion (PBF) methods have been widely used for metal and alloy printing [2]. PBF processes can be divided into selective laser melting (SLM) and electron beam melting (EBM). A group of engineering alloys widely used in different industries is stainless steels. They can be categorised into four main groups based on their microstructures: ferritic, martensitic and precipitation hardening (maraging), duplex and austenitic [3]. Here we focus on the printability of austenitic stainless steels such as 316L due to their wide application in industry and their susceptibility to microcrack and porosity formation during SLM.

SLM of austenitic stainless steels can be performed under a wide variety of process parameters including laser power (68–400 W), scan speed (0.3–2.5 m/s), layer thickness (20–50 μm), and hatch distance; the distance between the centre of two adjacent melt pools (40–140 μm) [4–15]. Therefore, depending on the process parameters, the alloy may experience a wide variety of temperature gradients, solidification conditions, thermal stresses, and be susceptible to defects such as cracks, pores, and residual stresses. In addition to the processing parameters, changes in the chemical composition of the powder can cause differences in solidification conditions and defect formation [16].

There are two main challenges upon the SLM of austenitic stainless steels: solidification cracking and porosity formation. In the case of solidification cracking, reports on the formation of hot cracks in SLM-produced 316L austenitic stainless steel point out the presence of impurity elements such

as silicon, phosphorus, and sulphur in the cracked regions [12,17–22]. Their synergistic impact with other alloying elements can lead to significant microsegregation during solidification and cause microcracking. Reported efforts to modify the chemical composition of austenitic stainless steels have led to improvements; however, such compositional changes are mainly based on welding literature and are circumscribed to such context [23].

As for porosity formation, some attempts intended to correlate process parameters to 316L as-built part density, both in laser metal deposition (LMD) and SLM [5,24]. Philo et al. [4] studied the formation of keyholes during SLM of 316L alloy using finite element method (FEM) at the mesoscale. Recently, Mukherjee et al. [2] used mechanistic models to study the printability of 316L stainless steel with a focus on lack of fusion. However, there is no comprehensive modelling approach to predict the formation of different types of porosity for different SLM parameters in austenitic stainless steels. Conventionally, numerous studies attempted to correlate the volumetric energy (heat input), which is the ratio between laser power P and scan speed v , layer thickness t and hatch distance h , to form porosity [25–27]. But, this expression does not consider the effects of material properties, and also other process parameters such as laser spot size. Therefore, other criteria for the prediction of porosity formation during SLM need to be developed.

Printability has traditionally been determined by trial and error experiments, so as to identify regions of successful material deposition. This approach is effective in producing high quality parts, but ignores the complex relationships between the thermal, physical, mechanical, chemical, and metallurgical processes involved. Moreover, the optimised process parameters obtained cannot be applied to other types of alloys or SLM machines. Therefore, this approach is time consuming, costly and not amenable to scaled adoption.

Although Empirical/trial and error approach is needed, but a physics-based understanding is also needed to account for both the properties of the alloy and the physics of the SLM process. Such models can be validated by experiments. In this work, the aim is to present a theory-based approach incorporating the effects of chemical composition and process parameters on defect formation during SLM. Using this approach, many physical and metallurgical aspects can be accounted for simultaneously and the best conditions for both composition and process parameters can be determined to print a component without critical defects. The proposed approach is validated with literature results, testing the methodology presented in this paper for the printability of a defect-free austenitic stainless steel.

2. Printability of Austenitic Stainless Steels

The critical defects that can cause problems in printing austenitic stainless steels are solidification cracking (hot cracking) and porosity (lack of fusion, balling, keyholing) [19,28–30]. Both the composition of the alloy and SLM parameters can affect formation of these defects. In the next sections, each of these defects and the factors that can affect them will be discussed.

2.1. Solidification Cracking

Solidification cracks can form in the melting zone due to the segregation of alloying elements. The susceptibility to solidification cracking can be quantified by defining the brittle temperature range (BTR), within which the volume fraction of the remaining liquid phase during solidification is less than 5% [31]. Figure 1 shows schematically the sequence of alloy solidification. The first solid forms from liquid and acts as a nucleus to which further atoms attach, forming a dendrite (Figure 1a). The dendrite size increases in forthcoming stages of solidification together with other dendrites until grains are formed (Figure 1b,c). Since alloys solidify over a range of temperatures, it can be assumed that the first metal to solidify displays the highest melting point composition, whilst the latest displays the lowest melting point composition, the eutectic composition. Consequently, the lowest melting point alloy composition is pushed ahead of the solidifying dendrite, until it becomes trapped in between the grain boundaries (Figure 1d). Therefore, a large difference between the melting point of the eutectic

and the bulk alloy results in an increase in solidification (hot) cracking susceptibility [32]. Therefore, the first criterion for designing crack-free austenitic stainless steels is to minimise the solidification temperature range (STR), the difference between liquidus and solidus temperatures.

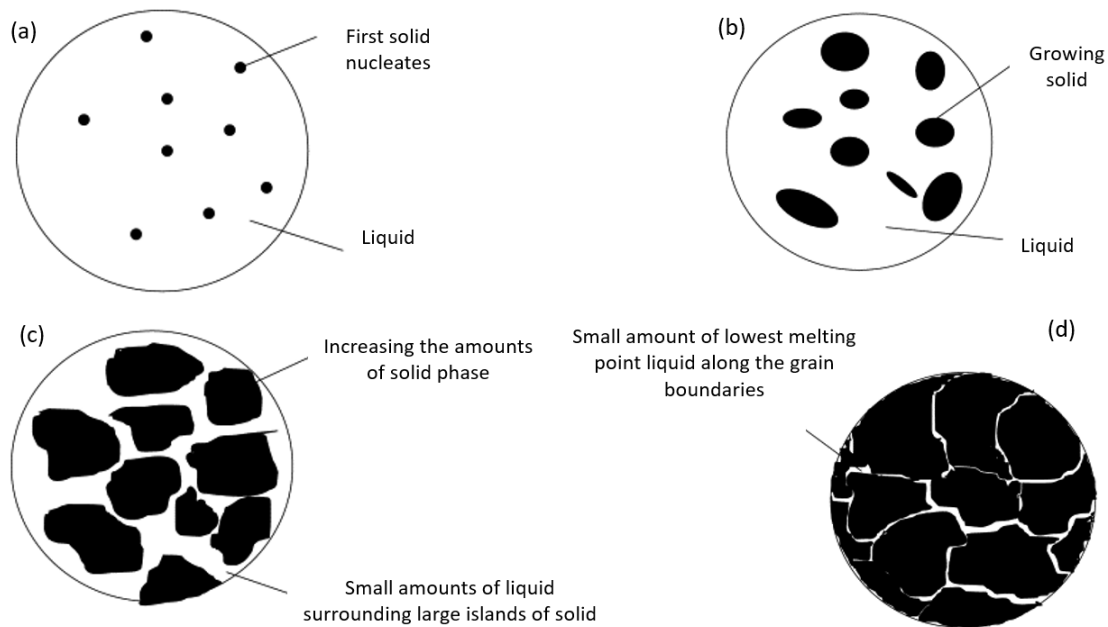


Figure 1. Schematic showing how an alloy solidifies. (a) The beginning of solidification (near liquidus temperature); (b) solid phase grows through the liquid phase; (c) the amount of solid increases by lowering temperature; (d) in the brittle temperature range, low amounts of liquid should remain along the grain boundaries of solid [32].

In addition to STR, the unique characteristics of the SLM can also affect the cracking behaviour of the alloy. During SLM, generated thermal stresses can be measured using Equation (1) [33]:

$$\sigma_{thermal} = \left[\frac{E \cdot \alpha_{CTE}}{2(1 - \nu)} \right] \Delta T \quad (1)$$

where E is the Young's modulus, α_{CTE} is the coefficient of thermal expansion, ν is the Poisson's ratio, and ΔT is the temperature difference on the surface being heated. Therefore, alloys with lower α_{CTE} display lower thermal stresses upon SLM. Focusing on the material properties, a performance index (PI) can be defined to rank the materials compared to each other [33]:

$$PI = \frac{\sigma_{ys}}{\alpha_{CTE}} \quad (2)$$

where σ_{ys} is the yield strength of the material; this can be defined as [34]:

$$\sigma_{ys} = \Delta\sigma_{gb} + \Delta\sigma_{ss} + \Delta\sigma_{pr} \quad (3)$$

where $\Delta\sigma_{gb}$ relates to the grain boundary hardening resulting from grain size, $\Delta\sigma_{ss}$ is the solid solution hardening, and $\Delta\sigma_{pr}$ is the precipitation hardening. The most important strengthening term in printing austenitic stainless steels is solid solution hardening, because precipitation is inhibited under fast cooling conditions. It can be calculated via [35]:

$$\Delta\sigma_{ss} = \left[\sum_i (k_{ss,i}^3 c_i) \right]^{\frac{2}{3}} \quad (4)$$

where $k_{ss,i}$ is the solid solution strengthening coefficient for element i and c_i is the volume fraction of the corresponding element i . Because the aim is stainless steel alloy design, only solid solution strengthening will be considered. In order to define PI , two terms of strength and coefficient of thermal expansion of the material should be calculated based on the chemical composition. $K_{ss,i}$ for different alloying elements in an austenitic matrix are presented in Table 1.

Table 1. Coefficients for solid solution hardening for different elements (i) in austenitic matrix [35], and their thermal expansion coefficient near their melting point [36].

i	Ni	Cr	Mo	W	C	N	Si	Fe (FCC)
$k_{ss,i}$ [MPa at% ^{-3/2}]	112	101.71	637	826	1984	1984	-	-
α_{CTE} [10^{-6} K ⁻¹]	20.3	19	16.5	11.6	-	-	3.8	23.3

α_{CTE} of a material can be calculated via a linear combination of the concentration of each alloying element and its corresponding coefficient [37]. The α_{CTE} of different elements at temperatures near their melting points are also listed in Table 1. Maximising the PI can lead to good thermal shock resistance and a reduction in crack formation, which is the second criterion for designing a crack-free austenitic stainless steel.

In welding literature, one way to assess the susceptibility of an austenitic stainless steel to cracking is the solidification mode. As in SLM the part will be built in layers, these layers should be bonded to each other. The third criterion adopted here stems from the welding literature, which can also help in reducing cracking. There are four solidification modes, based on the subsequent solid-state transformations [16] (Figure 2):

- (1) Austenitic (A) ($L \rightarrow L + \gamma \rightarrow \gamma$)
- (2) Austenitic-ferritic (AF) ($L \rightarrow L + \gamma \rightarrow L + \delta + \gamma \rightarrow \gamma + \delta$)
- (3) Ferritic-austenitic (FA) ($L \rightarrow L + \delta \rightarrow L + \delta + \gamma \rightarrow \gamma + \delta$)
- (4) Ferritic (F) ($L \rightarrow L + \delta \rightarrow \delta \rightarrow \delta + \gamma$)

In order to predict which mode dominates during solidification, the ratio of chromium equivalent and nickel equivalent has been widely adopted, as it determines the stability of δ -ferrite and austenite upon solidification. Different relationships have been proposed to account for those values [38–41]; however, the most comprehensive has been presented by Hull [42]:

$$Cr_{eq} = W_{Cr} + 1.21W_{Mo} + 0.48W_{Si} + 0.14W_{Nb} + 2.2W_{Ti} + 0.72W_W + 0.21W_{Ta} + 2.27W_V + 2.48W_{Al} \quad (5)$$

$$Ni_{eq} = W_{Ni} + 0.11W_{Mn} + 24.5W_C + 18.4W_N + 0.44W_{Cu} + 0.41W_{Co} \quad (6)$$

where W_i , $i = Cr, Mo, Si, W, Nb, \dots$ is the wt.% of element i .

The relationship between Cr_{eq}/Ni_{eq} and solidification modes has been depicted in Figure 2. When Cr_{eq}/Ni_{eq} is higher than 1.3, the presence of δ -ferrite is ensured during solidification [43], and if this ratio is higher than 1.4, the solidification mode will change from AF to FA [44]. It is widely accepted that the presence of δ -ferrite can improve solidification cracking resistance of austenitic stainless steels during welding, by reducing STR [45]. δ -ferrite has also a better ability than austenite to dissolve the impurity elements during solidification. Table 2 shows the partition coefficients of the most important impurity elements in austenitic stainless steels (Si, P, and S). Solute microsegregation increases significantly with decreasing the partition coefficient [46]. Therefore, these impurity elements can be dissolved in δ -ferrite, which can lead to a decrease in interdendritic segregation and a subsequent chance of solidification cracking. The presence of δ -ferrite during solidification is the basis of the third criterion for alloy design. It should be noted that δ -ferrite only is present during solidification and it will be transformed to austenite after solidification completion.

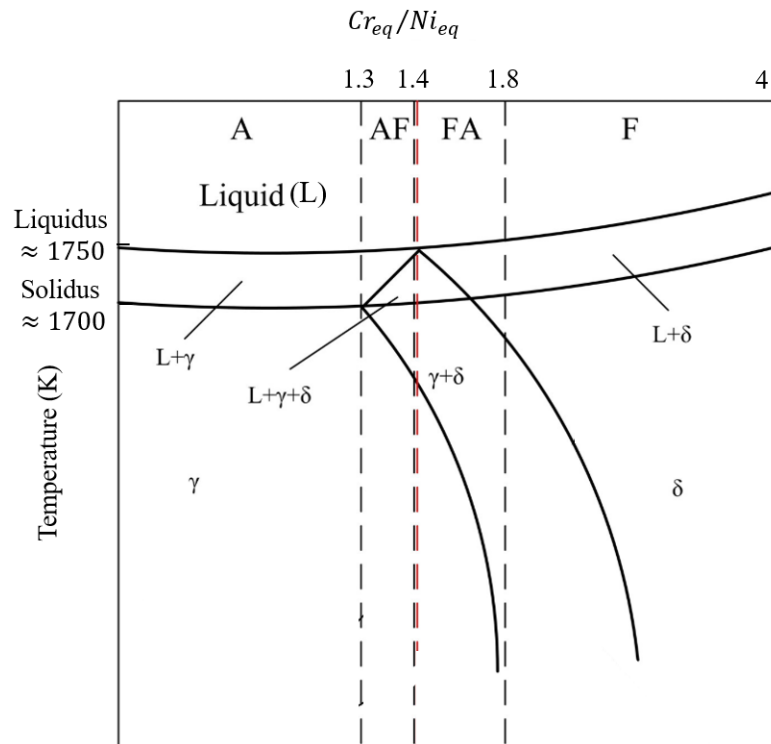


Figure 2. Solidification modes of austenitic stainless steels based on different Cr_{eq}/Ni_{eq} values.

Table 2. Partition coefficient of the most important impurity elements in austenite and δ -ferrite [23].

Impurity Element	Partition Coefficient in γ	Partition Coefficient in δ
Sulphur	0.035	0.091
Phosphorus	0.13	0.23
Silicon	0.52	0.77

2.2. Porosity Formation

Porosity can be detrimental to mechanical properties. Pores can be divided into two main categories: spherical and irregular shapes. Spherical pores can be attributed to gas entrapment during powder production [47], and are thought to be acceptable at the component level, with a maximum acceptable amount in the range of 0.7% [48]. Irregularly shaped pores are divided into three types: lack of fusion, keyhole and balling. Lack of fusion pores stem from insufficient penetration of the melt pool into the previous layer (Figure 3a) [49]. The keyhole effect is mostly due to very high heat inputs that can cause vapourisation and the formation of deep V-shape melt pools as can be seen in Figure 3b [50]. Balling is a periodic change in the size and shape of the solidified track, which is due to capillarity-driven instabilities of the melt pool. This phenomenon can lead to the formation of voids and problems for even powder spreading of the subsequent layers (Figure 3c) [51].

Irregularly shaped pores directly result from SLM processing parameters. Any changes in such parameters lead to a change in the melt pool geometry. Therefore, in order to predict porosity, the melt pool geometry should be predicted. Based on available data for additive manufacturing, laser processing, and welding, some thresholds for melt pool geometry and formation of each type of porosity can be defined. A schematic of the melt pool geometry is shown in Figure 4.

The lack of fusion threshold can be determined by two criteria. Firstly, the ratio between the depth of the melt pool (D) and the layer thickness of the process (t) [49]. Secondly, the ratio between hatch distance (h) and the width of the melt pool (W) can determine the good penetration of the melt pools on each other [30]. These conditions respectively dictate lack of fusion in the laser direction and normal to it.

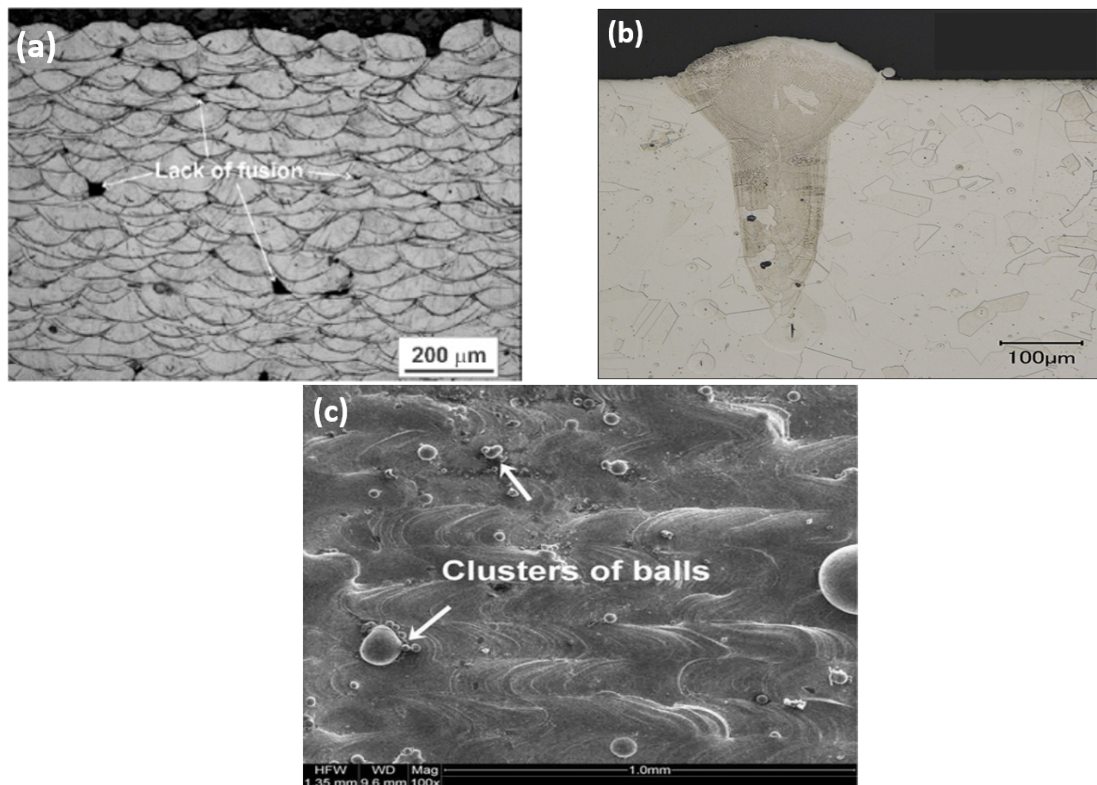


Figure 3. (a) Micrograph showing lack of fusion pores; (b) keyhole porosity [29]; (c) balling defect [52].

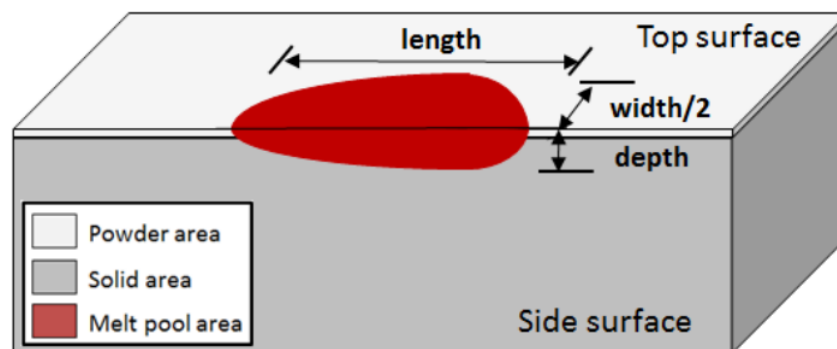


Figure 4. The schematics of the definition of melt pool depth (D), width (W), and length (L) [53].

The formation of keyholes can be predicted in two different ways. The ratio between width and depth of the melt pool determines the possibility of keyhole formation and secondly, based on the processing parameters and thermophysical properties such as enthalpy of melting of the alloy, the threshold energy for keyholing can be calculated [29]. Both stem from excess heat per unit volume, which can cause local evaporation.

The ratio between the length (L) and width of the melt pool also can define a criterion for balling, as the melt pool needs to uniformly redistribute the flow behind the advancing laser [54]. Quantitative expressions for these criteria will be presented in next sections.

3. Methodology

3.1. Optimisation of Chemical Composition for Crack Prevention

Three composition-dependent functions should be optimised. STR should be minimised, PI should be maximised, and Cr_{eq}/Ni_{eq} needs to be higher than 1.3, changing the chemical composition of the alloy.

3.2. Porosity Formation Prevention Criteria

For lack of fusion prevention, melt pool geometry must meet two semi-empirical conditions: $D/t > 1.5$ and $h/W < 1$ [30,49]. For balling prevention, the criterion is $L/W < 2.3$ [54]. For keyholing prevention two approaches exist. First criterion is $W/D > 2$. The second is based on the processing parameters and physical properties of the material. Using the concept of normalised enthalpy, the energy needed to avoid vapourisation and the formation of keyholes can be estimated [29]. The normalised enthalpy can be calculated via the following equation:

$$\frac{\Delta H}{h_s} = \frac{AP}{h_s \sqrt{\pi d v \sigma^3}} \quad (7)$$

where A is the powder absorptivity, P is the laser power, h_s is the enthalpy of melting, d is the thermal diffusivity, v is the laser scan speed, and σ is the laser spot size (the area covered by the laser). An estimate for keyhole threshold in terms of normalised enthalpy is $\frac{\Delta H}{h_s} > \frac{\pi T_b}{T_m}$ [29]. T_b and T_m are the boiling and melting temperatures, respectively. Using values for melting and vapourisation for austenitic stainless show that the threshold for keyhole formation in austenitic stainless steels is about 7.

To summarise, the defects listed above and their prevention means are presented in Table 3. Except from the balling prevention criterion, the same as reported in the literature, all the other criteria have been modified and compared with their origin. For the first time, criteria to avoid microcracking in SLM of austenitic stainless steels are presented. Conditions for lack of fusion, the criteria reported in literature have been modified to two distinct and simple criteria. For keyhole prevention, the appropriate use of the normalised enthalpy and the correct threshold have been presented here.

Table 3. The summary of the defects appearing during SLM and the criteria proposed in this study for avoiding them. The references and how this paper modified the criteria are also provided.

Phenomenon	Criteria	Ref.	Notes
Microcracks	STR minimisation		Imposed to reduce formation of low melting point eutectics
	PI maximisation		Defined as thermal shock resistance
	Presence of δ -ferrite during solidification		Alleviating detrimental effects of impurity elements
Lack of fusion	$D/t > 1.5$	[30]	A ratio of 1.1 has been suggested by Mukherjee et al.
	$h/W < 1$	[49]	Tang et al. claimed the criteria for lack of fusion prevention is $(h/W)^2 + (t/D)^2 < 1$
Keyholes	$W/D > 2$	[55]	Johnson et al. suggested a ratio of 1.5 rather than 2
	$\Delta H/h_s < 7$	[29]	King et al. suggested a threshold of 30 rather than 7
Balling	$L/W < 2.3$	[54]	-

Model for Melt Pool Dimensions

In order to predict the melt pool geometry based on different processing parameters, a combination of physical models which can relate the material properties to SLM processing parameters has been used.

The width of the melt pool (W) can be described by [56]:

$$W = \sqrt{\frac{8}{\pi e} \frac{AP}{\rho C_p v (T_m - T_0)}} \quad (8)$$

where ρ is the density, C_p is the heat capacity, and T_0 is the initial temperature of the powder bed.

For the melt pool depth (D) and length (L), the Eagar-Tsai model is a good estimation [57]. Firstly two dimensionless parameters of F and B should be introduced. F can be defined as the ratio between the laser dwell time and thermal diffusion time, which is:

$$F = \sqrt{\frac{d}{v\sigma}} \quad (9)$$

The second dimensionless parameter (B) is the ratio between laser deposited energy density and enthalpy of melting, which can be simplified as:

$$B = \frac{\Delta H}{2^{3/4}\pi h_s} \quad (10)$$

Both D and L are functions of B and F . The expressions that can be used for D and L predictions can be simplified into these final equations:

$$D = \frac{\sigma}{\sqrt{F}} \left[0.008 - 0.0048B - 0.047F - 0.099BF + (0.32 + 0.015B)F \ln F + \ln B(0.0056 - 0.89F + 0.29F \ln F) \right] \quad (11)$$

$$L = \frac{\sigma}{F^2} \left[0.0053 - 0.21F + 1.3F^2 + (-0.11 - 0.17B)F^2 \ln F + B(-0.0062 + 0.23F + 0.75F^2) \right] \quad (12)$$

The values for B and F are only valid for the materials that have $F < 1$, such as austenitic stainless steels. For materials which have $F > 1$, B and F should be measured in other ways discussed in [57], which is not the subject of this paper.

4. Model Validation

Experimental data on SLM of 316L stainless steel is presented next to relate chemical compositions and process parameters reported in the literature to different types of defects. The criteria for defect prevention are compared to the existing data in the literature, and their reliability is shown.

4.1. Cracking Behaviour of 316L Stainless Steel

As 316L alloy is an industrially relevant austenitic stainless steel due to its wide application, here we focus on the cracking behaviour of this type of steel. Table 4 lists different compositions of 316L stainless steel, which have been produced using SLM; in the first three printed parts (shown in bold) microcrack formation has been reported. STR, PI , and Cr_{eq}/Ni_{eq} are also calculated for each of these alloys. The first alloy in this list has an inappropriate solidification mode (A mode), the second alloy has high STR of 60 K, and the third alloy has a low PI of 1.19×10^6 MPa·K.

In order to reduce the cracking susceptibility, alterations in alloy composition of 316L stainless steel can be performed. Table 4 also shows 11 different variations of 316L compositions that have been printed successfully without microcracks being reported. All of these alloys solidify in FA mode. Furthermore, there is a compromise between STR, PI and Cr_{eq}/Ni_{eq} in all cases. When STR is lower than 39 K, the alloys show a safe solidification behaviour, no matter what is their PI and Cr_{eq}/Ni_{eq} . However, when STR is equal or higher than 39 K, the situation gets more complicated. For the alloys printed in [5,58], high PI compensates the wide solidification temperature range. For the three last alloys listed in Table 4, the low PI will be compensated by high Cr_{eq}/Ni_{eq} values, which is indicative of higher δ -ferrite during solidification. The minimum STR and maximum PI that have been reported in the literature is 32 K and 1.46×10^6 MPa·K, respectively, which can be used as metrics for designing new alloy formulations.

Table 4. Chemical compositions of 316L stainless steel produced by SLM. The units of STR and *PI* are K and MPa·K, respectively. Fe contents are balanced and not shown in the table. The alloys in bold font underwent cracking.

Cr	Ni	Mn	Mo	C	N	Si	P	S	STR	<i>PI</i> × 10 ⁶	<i>Cr_{eq}</i> / <i>Ni_{eq}</i>	Ref.
16.17	12.57	0.23	2.33	0.098	-	0.6	0.014	0.014	50	1.32	1.28	[17]
20.7	11.4	1.32	2.45	0.02	0.09	0.5	0.02	0.01	60	1.46	1.58	[19]
17.26	11.48	1.41	2.32	0.018	-	0.71	0.01	0.01	39	1.19	1.68	[12]
17.34	10.74	1.14	2.28	0.01	0.1	0.63	0.026	0.014	43	1.36	1.57	[5]
17.5	11.5	2	2.25	0.03	0.11	1	0.045	0.03	57	1.45	1.54	[58]
17.42	12.53	0.6	2.36	0.02	0.06	0.51	0.01	0.01	32	1.36	1.45	[8]
17	12	1	2.5	0.015	0.05	0.5	0.023	0.01	38	1.35	1.51	[59]
17.75	12.75	1.5	2.4	0.02	-	-	0.01	0.001	33	1.24	1.49	[10]
16.7	11.9	0.6	2.5	0.02	-	0.6	0.01	0.02	33	1.22	1.61	[11]
16.7	10.3	0.99	2.2	0.01	-	0.69	0.02	0.05	37	1.12	1.85	[60]
17.9	12.8	1.15	2.35	0.018	0.09	0.66	0.01	0.004	33	1.42	1.4	[61]
17.5	11.2	2.2	2.3	0.03	-	-	0.05	0.03	61	1.22	1.67	[62]
16.3	10.3	1.31	2.09	0.026	-	0.49	0.026	0.006	44	1.14	1.72	[14]
18.43	12.2	1.86	2.46	0.02	-	0.75	0.032	0.01	54	1.26	1.69	[15]

4.2. Porosity and Defect Formation Behaviour of 316L Stainless Steel

As processing parameters are the most important factor that can affect the formation of porosity during SLM, several attempts have been made on their optimisation to maximise part densities. Table 5 shows the different combinations of SLM processing parameters and their reported melt pool dimensions as well as the predicted porosity types based on the criteria presented in this paper, and the real observations. The normalised enthalpy for each of the process parameter sets is calculated whenever the alloy composition and SLM machine parameters are reported. The criteria mentioned in 3.2 not only can predict the formation of pores based on the melt pool dimensions, but also the exact types of defects after manufacturing. In all cases that the model predicts formation of specific pores, the percentage of pores is more than 0.1%. For alloy number 3, where no pores are predicted by the criteria presented here, a perfect build has been reported. The normalised enthalpy values for alloy 3 is below the critical value of 7, which shows the reliability of using this concept for keyhole prevention. The alloys with normalised enthalpies higher than 7 underwent keyhole formation. Occurrence of lack of fusion and balling were also as expected based on the criteria mentioned before in this paper. In order to show the inability for the conventional methods to predict porosity, the volumetric energy ($\frac{P}{v \cdot h \cdot t}$) has been plotted for each of full-reported sets of experiments in Table 5 and shown in Figure 5. It is seen that volumetric energy cannot be correlated with pore formation. The reason is that in addition to laser power, scan speed, layer thickness, and hatch distance, the laser spot size should be considered as an important variable of SLM that can affect the density of the as-built part. Moreover, the volumetric energy cannot consider the effects of material properties on the formation of pores.

Based on the model presented in this paper for porosity prevention, the laser spot size and the enthalpy of melting of the alloy are amongst the two most important parameters that can affect porosity and defects. Figure 6 shows the variations of these two values based on a change in chemical composition of the alloy and the SLM machines (for alloys number 1–4 of Table 5). Even small changes in chemical composition can cause large differences in enthalpy of melting of the alloy and the resulting pore percentage, which has been ignored in conventional approaches for porosity prediction. Moreover, laser spot size variations can significantly affect the keyhole formation (by changing the normalised enthalpy values) and melt pool depth and length. Therefore, instead of the conventional approach to estimate the part density after SLM, the methodology presented here can lead to a precise estimation about the density of the SLM as-built parts.

Table 5. SLM processing parameters including P (W), v (mm/s), t (μm), and h (μm) that have been used for production of 316L stainless steel in four different studies. For each set of experiments the measured melt pool dimensions L (μm), W (μm), and D (μm) (or some of them) and their related normalised enthalpies have been presented. The variables represented by dashes, have not been reported in the original reference. In cases where the laser spot size or the full composition were not reported, $\Delta H/h_s$ could not be calculated and N/A is shown. The prediction about lack of fusion (LOF), keyhole formation (K), balling (B) and experimental measurements are also presented.

Alloy	P	V	t	h	L	W	D	$\Delta H/h_s$	Prediction	Pores	Ref.
1	200	850	30	90	-	146	110	N/A	K	0.4 %	[63]
1	200	1000	30	90	-	130	85	N/A	K	0.5 %	[63]
1	200	1150	30	90	-	104	85	N/A	K	0.45 %	[63]
1	200	1300	30	90	-	104	70	N/A	K	0.85 %	[63]
1	200	1450	30	90	-	104	75	N/A	K	1.7 %	[63]
1	200	1600	30	90	-	100	70	N/A	K	2.5 %	[63]
2	100	100	50	40	-	180	30	N/A	LOF	Not reported	[64]
2	100	200	50	40	-	140	20	N/A	LOF	Not reported	[64]
2	100	300	50	40	-	120	10	N/A	LOF	Not reported	[64]
2	100	400	50	40	-	110	5	N/A	LOF	Not reported	[64]
3	175	500	30	140	-	175	75	6.9	No pores	No pores	[65]
3	400	1100	30	140	-	250	110	4.3	No pores	No pores	[65]
4	250	1500	-	-	526	105.6	52.8	41.8	B	0.9 %	[66]
4	250	1800	-	-	523.5	100.8	48	38.2	B	1.39 %	[66]
4	400	1800	-	-	846.4	129.6	60	61.1	B	1.2 %	[66]
4	100	400	-	-	212.4	129.6	59.5	32.4	No B/K	0.93 %	[66]
5	400	1800	30	112	32	112	105	8.7	K	0.5 %	[67]
5	400	1500	30	112	79	103	119	9.4	LOF/K	0.8 %	[67]
5	300	1800	30	112	57	94	65	7.1	LOF/K	0.7 %	[67]
5	300	1500	30	112	35	83	94	7.5	LOF/K	0.7 %	[67]
5	200	1500	30	112	26	84	57	6.9	LOF/K	1.3 %	[67]
5	200	1200	30	112	45	104	68	7.1	LOF/K	0.5 %	[67]
5	200	800	30	112	24	123	116	7.3	K	1.3 %	[67]
5	150	1200	30	112	21	79	30	5.12	LOF	4.5 %	[67]
5	150	800	30	112	44	109	67	6.8	LOF/K	1.5 %	[67]
5	150	500	30	112	40	115	120	7.8	K	1 %	[67]

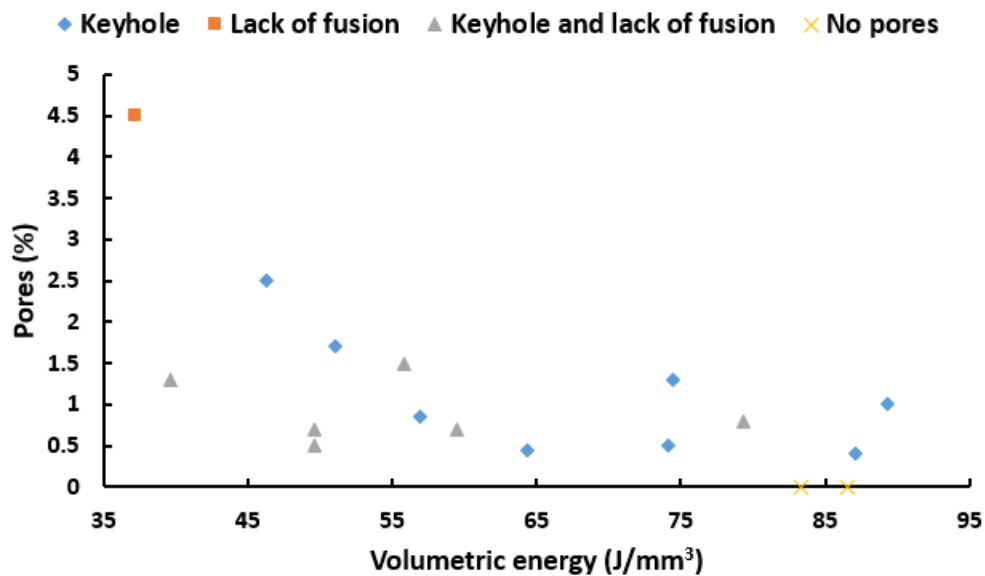


Figure 5. Porosity map that shows the experimental porosity percentage for some of the alloys presented in Table 4, based on the volumetric energy. The predictions of the proposed model in this diagram are also included in this diagram.

Some works have tried to simulate the melt pool geometry of SLM-produced 316L stainless steel, using finite element methods [2,68]. However, because of the complexity of heat transfer phenomena and the differences between physical properties of the powder and the bulk material, the FEM simulations suffer from precision. Furthermore, these methods are expensive and time consuming. Most of finite element simulations set some of the SLM parameters as constants and try to simulate the process. Although the new methodology presented in this paper assumes many simplifications and some of the heat transfer phenomena are neglected, but it can predict melt pool geometry in an economic and time consuming manner and can provide part producers a good overview for choosing the right processing parameters whilst accounting for compositional variations.

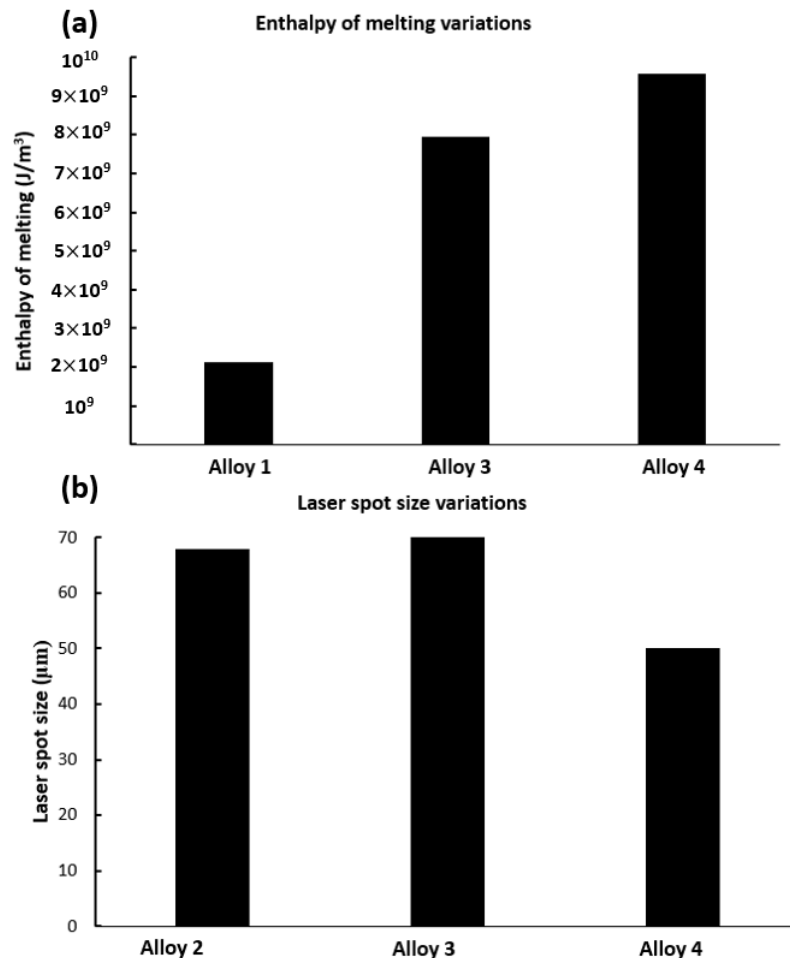


Figure 6. (a) Huge differences of the enthalpy of melting of the alloys 1, 3, and 4 of the Table 5. (b) Different laser spot sizes that have been used to build the alloys 2, 3, and 4 of the Table 4.

5. Summary and Conclusions

A novel methodology has been presented to predict the formation of two most important issues during selective laser melting of austenitic stainless steels: solidification cracking and porosity formation. In the case of solidification cracking, three functions of solidification temperature range (difference between liquidus and solidus temperature), the performance index (ratio between the yield strength and coefficient of thermal expansion of the material), and Cr_{eq}/Ni_{eq} (determining the solidification path) have been presented as metrics to predict the possibility of cracking. The minimisation of the solidification temperature range, the maximisation of performance index, and the presence of δ -ferrite during solidification predict the minimisation of solidification cracking

susceptibility. The criteria defined in this paper have been compared to existing data in literature for selective laser melted 316L stainless steel.

In the case of porosity formation, different criteria which correlate SLM processing parameters and the physical properties of the material with the quality of formation of melt pool and solidification behaviour have been defined. A novel physical model has been suggested to predict the conditions for keyhole formation and also the melt pool geometry. The proposed criteria have been compared with literature data on SLM of 316L alloy showing remarkable agreement.

Author Contributions: H.E.S. wrote the manuscript, gathered data from literature, proposed the methodology and validated the model; P.E.J.R.-D.-d.-C. supervised the whole process, guiding the model development and validation, and revising the manuscript.

Funding: This study has been funded by the Royal Academy of Engineering (RCSRF1718/5/32) and EPSRC via DARE grant (EP/L025213/1).

Acknowledgments: The authors are grateful to Carpenter Additive for useful discussions. To the Royal Academy of Engineering for chair funding (RCSRF1718/5/32), and to the EPSRC for funding via DARE grant (EP/L025213/1). The authors are grateful to Will Herbert from Carpenter Additive for useful comments.

Conflicts of Interest: The authors declare no conflict of interest.

References

1. DebRoy, T.; Wei, H.; Zuback, J.; Mukherjee, T.; Elmer, J.; Milewski, J.; Beese, A.; Wilson-Heid, A.; De, A.; Zhang, W. Additive manufacturing of metallic components—Process, structure and properties. *Prog. Mater. Sci.* **2018**, *92*, 112–224. [[CrossRef](#)]
2. Mukherjee, T.; DebRoy, T. Printability of 316 stainless steel. *Sci. Technol. Weld. Join.* **2019**, *24*, 412–419. [[CrossRef](#)]
3. Lippold, J.C.; Kotecki, D.J. Welding metallurgy and weldability of stainless steels. In *Welding Metallurgy and Weldability of Stainless Steels*; Lippold, J.C., Kotecki, D.J., Eds.; Wiley-VCH: Weinheim, Germany, 2005; p. 376, ISBN 0-471-47379-0.
4. Philo, A.; Mehraban, S.; Holmes, M.; Sillars, S.; Sutcliffe, C.; Sienz, J.; Brown, S.; Lavery, N. A pragmatic continuum level model for the prediction of the onset of keyholing in laser powder bed fusion. *Int. J. Adv. Manuf. Technol.* **2019**, *101*, 697–714. [[CrossRef](#)]
5. Bertoli, U.S.; MacDonald, B.E.; Schoenung, J.M. Stability of cellular microstructure in laser powder bed fusion of 316L stainless steel. *Mater. Sci. Eng. A* **2019**, *739*, 109–117. [[CrossRef](#)]
6. Evans, J.A.; Anderson, S.A.; Faierson, E.J.; Perez-Nunez, D.; McDeavitt, S.M. Anisotropic Radiation-Induced Changes in Type 316L Stainless Steel Rods Built by Laser Additive Manufacturing. *Nucl. Technol.* **2019**, *205*, 563–581. [[CrossRef](#)]
7. Heiden, M.J.; Deibler, L.A.; Rodelas, J.M.; Koepke, J.R.; Tung, D.J.; Saiz, D.J.; Jared, B.H. Evolution of 316L stainless steel feedstock due to laser powder bed fusion process. *Addit. Manuf.* **2019**, *25*, 84–103. [[CrossRef](#)]
8. Obeidi, M.A.; McCarthy, E.; O'Connell, B.; Ul Ahad, I.; Brabazon, D. Laser Polishing of Additive Manufactured 316L Stainless Steel Synthesized by Selective Laser Melting. *Materials* **2019**, *12*, 991. [[CrossRef](#)]
9. Song, M.; Wang, M.; Lou, X.; Rebak, R.B.; Was, G.S. Radiation damage and irradiation-assisted stress corrosion cracking of additively manufactured 316L stainless steels. *J. Nucl. Mater.* **2019**, *513*, 33–44. [[CrossRef](#)]
10. Yang, Y.; Zhu, Y.; Khonsari, M.; Yang, H. Wear anisotropy of selective laser melted 316L stainless steel. *Wear* **2019**, *428*, 376–386. [[CrossRef](#)]
11. Yin, Y.; Sun, J.; Guo, J.; Kan, X.; Yang, D. Mechanism of high yield strength and yield ratio of 316 L stainless steel by additive manufacturing. *Mater. Sci. Eng. A* **2019**, *744*, 773–777. [[CrossRef](#)]
12. Chen, W.; Yin, G.; Feng, Z.; Liao, X. Effect of Powder Feedstock on Microstructure and Mechanical Properties of the 316L Stainless Steel Fabricated by Selective Laser Melting. *Metals* **2018**, *8*, 729. [[CrossRef](#)]
13. Montero-Sistiaga, M.L.; Godino-Martinez, M.; Boschmans, K.; Kruth, J.P.; Van Humbeek, J.; Vanmeensel, K. Microstructure evolution of 316L produced by HP-SLM (high power selective laser melting). *Addit. Manuf.* **2018**, *23*, 402–410. [[CrossRef](#)]

14. Yan, F.; Xiong, W.; Faierson, E.; Olson, G.B. Characterization of nano-scale oxides in austenitic stainless steel processed by powder bed fusion. *Scr. Mater.* **2018**, *155*, 104–108. [[CrossRef](#)]
15. Yusuf, S.M.; Nie, M.; Chen, Y.; Yang, S.; Gao, N. Microstructure and corrosion performance of 316L stainless steel fabricated by Selective Laser Melting and processed through high-pressure torsion. *J. Alloy Compd.* **2018**, *763*, 360–375. [[CrossRef](#)]
16. Yu, J.; Rombouts, M.; Maes, G. Cracking behavior and mechanical properties of austenitic stainless steel parts produced by laser metal deposition. *Mater. Des.* **2013**, *45*, 228–235. [[CrossRef](#)]
17. Röttger, A.; Geenen, K.; Windmann, M.; Binner, F.; Theisen, W. Comparison of microstructure and mechanical properties of 316 L austenitic steel processed by selective laser melting with hot-isostatic pressed and cast material. *Mater. Sci. Eng. A* **2016**, *678*, 365–376. [[CrossRef](#)]
18. Geenen, K.; Röttger, A.; Theisen, W. Corrosion behavior of 316L austenitic steel processed by selective laser melting, hot-isostatic pressing, and casting. *Mater. Corros.* **2017**, *68*, 764–775. [[CrossRef](#)]
19. Gray, G.T., III; Livescu, V.; Rigg, P.; Trujillo, C.P.; Cady, C.M.; Chen, S.R.; Carpenter, J.S.; Lienert, T.J.; Fensin, S.J. Structure/property (constitutive and spallation response) of additively manufactured 316L stainless steel. *Acta Mater.* **2017**, *138*, 140–149. [[CrossRef](#)]
20. Zhang, M.; Sun, C.N.; Zhang, X.; Goh, P.C.; Wei, J.; Hardacre, D.; Li, H. Fatigue and fracture behaviour of laser powder bed fusion stainless steel 316L: Influence of processing parameters. *Mater. Sci. Eng. A* **2017**, *703*, 251–261. [[CrossRef](#)]
21. Wang, W.H.; Liu, X.Y. Effect of linear energy density on pores of 316L stainless steel by selective laser melting. *IOP Conf. Ser. Earth Environ. Sci.* **2019**, *233*, 032008. [[CrossRef](#)]
22. Zhong, Y.; Liu, L.; Wikman, S.; Cui, D.; Shen, Z. Intragranular cellular segregation network structure strengthening 316L stainless steel prepared by selective laser melting. *J. Nucl. Mater.* **2016**, *470*, 170–178. [[CrossRef](#)]
23. Shankar, V.; Gill, T.; Mannan, S.; Sundaresan, S. Solidification cracking in austenitic stainless steel welds. *Sadhana* **2003**, *28*, 359–382. [[CrossRef](#)]
24. Pang, J.H.L.; Kaminski, J.; Pepin, H. Characterisation of porosity, density, and microstructure of directed energy deposited stainless steel AISI 316L. *Addit. Manuf.* **2019**, *25*, 286–296.
25. Gong, H.; Rafi, K.; Gu, H.; Starr, T.; Stucker, B. Analysis of defect generation in Ti–6Al–4V parts made using powder bed fusion additive manufacturing processes. *Addit. Manuf.* **2014**, *1*, 87–98. [[CrossRef](#)]
26. Ciurana, J.; Hernandez, L.; Delgado, J. Energy density analysis on single tracks formed by selective laser melting with CoCrMo powder material. *Int. J. Adv. Manuf. Technol.* **2013**, *68*, 1103–1110. [[CrossRef](#)]
27. Gunenthiram, V.; Peyre, P.; Schneider, M.; Dal, M.; Coste, F.; Koutiri, I.; Fabbro, R. Experimental analysis of spatter generation and melt-pool behavior during the powder bed laser beam melting process. *J. Mater. Process. Technol.* **2018**, *251*, 376–386. [[CrossRef](#)]
28. Gu, D.D.; Meiners, W.; Wissenbach, K.; Poprawe, R. Laser additive manufacturing of metallic components: Materials, processes and mechanisms. *Int. Mater. Rev.* **2012**, *57*, 133–164. [[CrossRef](#)]
29. King, W.E.; Barth, H.D.; Castillo, V.M.; Gallegos, G.F.; Gibbs, J.W.; Hahn, D.E.; Kamath, C.; Rubenchik, A.M. Observation of keyhole-mode laser melting in laser powder-bed fusion additive manufacturing. *J. Mater. Process. Technol.* **2014**, *214*, 2915–2925. [[CrossRef](#)]
30. Mukherjee, T.; Zuback, J.; De, A.; Reports, T.D.S. Printability of alloys for additive manufacturing. *Sci. Rep.* **2016**, *6*, 19717. [[CrossRef](#)]
31. Menou, E.; Ramstein, G.; Bertrand, E.; Tancret, F. Multi-objective constrained design of nickel-base superalloys using data mining-and thermodynamics-driven genetic algorithms. *Model. Simul. Mater. Sci. Eng.* **2016**, *24*, 055001. [[CrossRef](#)]
32. Mathers, G. *The Welding of Aluminium and Its Alloys*; Woodhead Publishing: Sawston, Cambridge, MA, USA, 2002.
33. Hunt, J.; Derguti, F.; Todd, I. Selection of steels suitable for additive layer manufacturing. *Ironmak. Steelmak.* **2014**, *41*, 254–256. [[CrossRef](#)]
34. Xu, W.; Rivera-Díaz-del Castillo, P.; Van Der Zwaag, S. Computational design of UHS maraging stainless steels incorporating composition as well as austenitisation and ageing temperatures as optimisation parameters. *Philos. Mag.* **2009**, *89*, 1647–1661. [[CrossRef](#)]
35. Toda-Caraballo, I.; Rivera-Díaz-del Castillo, P.E. Modelling solid solution hardening in high entropy alloys. *Acta Mater.* **2015**, *85*, 14–23. [[CrossRef](#)]
36. Cervera, F. *ASM Ready Reference: Thermal Properties of Metals*; ASM International: Novelty, OH, USA, 2002.

37. Toda-Caraballo, I.; Galindo-Nava, E.I.; Rivera-Díaz-del Castillo, P.E. Unravelling the materials genome: Symmetry relationships in alloy properties. *J. Alloy Compd.* **2013**, *566*, 217–228. [[CrossRef](#)]
38. Schaeffler, A.L. Constitution diagram for stainless steel weld metal. *Met. Prog.* **1949**, *56*, 680.
39. Long, C. The ferrite content of austenitic stainless steel weld metal. *Weld. J.* **1973**, *52*, 281s–297s.
40. Kotecki, D.; Siewert, T. WRC-1992 constitution diagram for stainless steel weld metals: A modification of the WRC-1988 diagram. *Weld. J.* **1992**, *71*, 171–178.
41. Hammar, O. Influence of steel composition on segregation and microstructure during solidification of austenitic stainless steels. *Solidif. Cast. Met.* **1979**, *401*.
42. Hull, F. Delta ferrite and martensite formation in stainless steels. *Weld. J.* **1973**, *52*, 193.
43. Faulkner, R.; Williams, J.; Sanchez, E.G.; Marshall, A. Influence of Co, Cu and W on microstructure of 9% Cr steel weld metals. *Mater. Sci. Technol.* **2003**, *19*, 347–354. [[CrossRef](#)]
44. Suutala, N. Effect of manganese and nitrogen on the solidification mode in austenitic stainless steel welds. *Metall. Trans. A* **1982**, *13*, 2121–2130. [[CrossRef](#)]
45. Pellini, W. Strain theory of hot tearing. *Foundry* **1952**, *80*, 125–133.
46. Huang, Y.; Long, M.; Liu, P.; Chen, D.; Chen, H.; Gui, L.; Liu, T.; Yu, S. Effects of partition coefficients, diffusion coefficients, and solidification paths on microsegregation in Fe-based multinary alloy. *Metall. Mater. Trans. B* **2017**, *48*, 2504–2515. [[CrossRef](#)]
47. Eskandari Sabzi, H. Powder bed fusion additive layer manufacturing of titanium alloys. *Mater. Sci. Technol.* **2019**, *35*, 875–890. [[CrossRef](#)]
48. Prithivirajan, V.; Sangid, M.D. The role of defects and critical pore size analysis in the fatigue response of additively manufactured IN718 via crystal plasticity. *Mater. Des.* **2018**, *150*, 139–153. [[CrossRef](#)]
49. Tang, M.; Pistorius, P.C.; Beuth, J.L. Prediction of lack-of-fusion porosity for powder bed fusion. *Addit. Manuf.* **2017**, *14*, 39–48. [[CrossRef](#)]
50. Lee, J.Y.; Ko, S.H.; Farson, D.F.; Yoo, C.D. Mechanism of keyhole formation and stability in stationary laser welding. *J. Phys. D Appl. Phys.* **2002**, *35*, 1570. [[CrossRef](#)]
51. Taheri, H.; Shoaib, M.R.B.M.; Koester, L.; Bigelow, T.; Collins, P.C.; Bond, L.J. Powder-based additive manufacturing—a review of types of defects, generation mechanisms, detection, property evaluation and metrology. *Int. J. Addit. Subtract. Mater. Manuf.* **2017**, *1*, 172. [[CrossRef](#)]
52. Zhang, L.C.; Attar, H.; Calin, M.; Eckert, J. Review on manufacture by selective laser melting and properties of titanium based materials for biomedical applications. *Mater. Technol.* **2016**, *31*, 66–76. [[CrossRef](#)]
53. Cheng, B.; Chou, K. Melt pool geometry simulations for powder-based electron beam additive manufacturing. In Proceedings of the 24th Annual International Solid Freeform Fabrication Symposium—An Additive Manufacturing Conference, Austin, TX, USA, 12–14 August 2013; pp. 644–654.
54. Ion, J.C.; Shercliff, H.R.; Ashby, M.F. Diagrams for laser materials processing. *Acta Metall. Mater.* **1992**, *40*, 1539–1551. [[CrossRef](#)]
55. Johnson, L.; Mahmoudi, M.; Zhang, B.; Seede, R.; Maier, J.T.; Maier, H.J.; Karaman, I.; Elwany, A.; Arroyave, R. Assessing Printability Maps in Additive Manufacturing of Metal Alloys. *Acta Mater.* **2019**, *176*, 199–210. [[CrossRef](#)]
56. Promoppatum, P.; Yao, S.C.; Pistorius, P.C.; Rollett, A.D. A comprehensive comparison of the analytical and numerical prediction of the thermal history and solidification microstructure of Inconel 718 products made by laser powder-bed fusion. *Engineering* **2017**, *3*, 685–694. [[CrossRef](#)]
57. Rubenchik, A.M.; King, W.E.; Wu, S.S. Scaling laws for the additive manufacturing. *J. Mater. Process. Technol.* **2018**, *257*, 234–243. [[CrossRef](#)]
58. Elangeswaran, C.; Cutolo, A.; Muralidharan, G.K.; de Formanoir, C.; Berto, F.; Vanmeensel, K.; Van Hooreweder, B. Effect of post-treatments on the fatigue behaviour of 316L stainless steel manufactured by laser powder bed fusion. *Int. J. Fatigue* **2019**, *123*, 31–39. [[CrossRef](#)]
59. Shrestha, R.; Simsirivong, J.; Shamsaei, N. Fatigue behavior of additive manufactured 316L stainless steel parts: Effects of layer orientation and surface roughness. *Addit. Manuf.* **2019**, *28*, 23–38. [[CrossRef](#)]
60. Harun, W.; Asri, R.; Romlay, F.; Sharif, S.; Jan, N.; Tsumori, F. Surface characterisation and corrosion behaviour of oxide layer for SLMed-316L stainless steel. *J. Alloy Compd.* **2018**, *748*, 1044–1052. [[CrossRef](#)]
61. Kunkel, M.H.; Gebhardt, A.; Mpofu, K.; Kallweit, S. Statistical assessment of mechanical properties of selective laser melted specimens of stainless steel. *Int. J. Adv. Manuf. Technol.* **2018**, *98*, 1409–1431. [[CrossRef](#)]

62. Lodhi, M.; Deen, K.; Haider, W. Corrosion behavior of additively manufactured 316L stainless steel in acidic media. *Materialia* **2018**, *2*, 111–121. [[CrossRef](#)]
63. Heeling, T.; Cloots, M.; Wegener, K. Melt pool simulation for the evaluation of process parameters in selective laser melting. *Addit. Manuf.* **2017**, *14*, 116–125. [[CrossRef](#)]
64. Masmoudi, A.; Bolot, R.; Coddet, C. Investigation of the laser–powder–atmosphere interaction zone during the selective laser melting process. *J. Mater. Process. Technol.* **2015**, *225*, 122–132. [[CrossRef](#)]
65. Andreau, O.; Koutiri, I.; Peyre, P.; Penot, J.D.; Saintier, N.; Pessard, E.; De Terris, T.; Dupuy, C.; Baudin, T. Texture control of 316L parts by modulation of the melt pool morphology in selective laser melting. *J. Mater. Process. Technol.* **2019**, *264*, 21–31. [[CrossRef](#)]
66. Wu, A.S.; Brown, D.W.; Kumar, M.; Gallegos, G.F.; King, W.E. An experimental investigation into additive manufacturing-induced residual stresses in 316L stainless steel. *Metall. Mater. Trans. A* **2014**, *45*, 6260–6270. [[CrossRef](#)]
67. Kamath, C.; El-dasher, B.; Gallegos, G.F.; King, W.E.; Sisto, A. Density of additively-manufactured, 316L SS parts using laser powder-bed fusion at powers up to 400 W. *Int. J. Adv. Manuf. Technol.* **2014**, *74*, 65–78. [[CrossRef](#)]
68. Bidare, P.; Bitharas, I.; Ward, R.; Attallah, M.; Moore, A.J. Fluid and particle dynamics in laser powder bed fusion. *Acta Mater.* **2018**, *142*, 107–120. [[CrossRef](#)]



© 2019 by the authors. Licensee MDPI, Basel, Switzerland. This article is an open access article distributed under the terms and conditions of the Creative Commons Attribution (CC BY) license (<http://creativecommons.org/licenses/by/4.0/>).